

You Only Label Once: 3D Box Adaptation from Point Cloud to Image via Semi-Supervised Learning

Jieqi Shi¹, Peiliang Li*², Xiaozhi Chen², Shaojie Shen¹

¹The Hong Kong University of Science and Technology, ²DJI

Abstract

The image-based 3D object detection task expects that the predicted 3D bounding box has a “tightness” projection (also referred to as cuboid), which fits the object contour well on the image while still keeping the geometric attribute on the 3D space, e.g., physical dimension, pairwise orthogonal, etc. These requirements bring significant challenges to the annotation. Simply projecting the Lidar-labeled 3D boxes to the image leads to non-trivial misalignment, while directly drawing a cuboid on the image cannot access the original 3D information. In this work, we propose a learning-based 3D box adaptation approach that automatically adjusts minimum parameters of the 360° Lidar 3D bounding box to perfectly fit the image appearance of panoramic cameras. With only a few 2D boxes annotation as guidance during the training phase, our network can produce accurate image-level cuboid annotations with 3D properties from Lidar boxes. We call our method “you only label once”, which means labeling on the point cloud once and automatically adapting to all surrounding cameras. As far as we know, we are the first to focus on image-level cuboid refinement, which balances the accuracy and efficiency well and dramatically reduces the labeling effort for accurate cuboid annotation. Extensive experiments on the public Waymo and NuScenes datasets show that our method can produce human-level cuboid annotation on the image without needing manual adjustment.

1. Introduction

Detecting accurate and well-aligned 3D bounding boxes from the image is one of the primary tasks for self-driving or augmented reality applications. Until now, keeping tuning the 3D detection accuracy from the network side has become more struggling and received less and less cost-performance ratio after several years of research efforts. Recently, the community has turned part of interests to scaling up the datasets to improve the model’s robustness and generalization ability [3, 21]. Therefore, efficient ground-truth annotation with high quality is becoming increasingly criti-

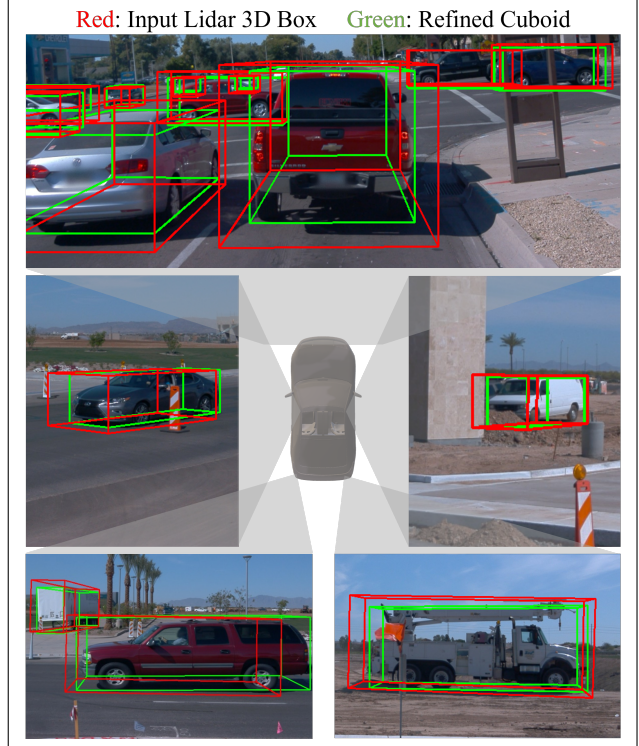


Figure 1. The image projection of the 3D bounding boxes **before** and **after** refinement, where we show five different camera views from the Waymo validation set as illustration. Our network can deal well with dislocation, tailing, and different viewpoints and generate 3D cuboids that align well with 2D areas.

cal [18, 23].

However, labeling accurate 3D boxes on visual data is heavily labor-consuming due to the degree of freedom (DoF) complexity and 3D information loss. Currently, there are mainly two ways to obtain the 3D bounding box annotation for image data. The first method tries reconstructing the object-centric point cloud from sequential images input [1], and then using the point clouds to guide the annotation. However, the static assumption in reconstruction-based approaches limits its application for dynamic objects in large-

scale self-driving scenarios. An alternative approach is rendering differentiable shape models for each object from single depth input [24]. But the frame-independent rendering cannot guarantee temporal consistency. Actually, both the reconstruction and rendering focus on dense pixel-level shape recovery, which requires much more computation than pure sparse 3D bounding box representation.

The second widely adopted way is labeling 3D bounding boxes on the Lidar point cloud [3, 21], then projecting the 3D boxes onto the image as the supervision signal for image-based 3D detection network. However, there are many challenges to obtaining accurate image cuboid annotation from Lidar 3D boxes, such as sensor timestamp synchronization, perfect extrinsic calibration for the whole image area. Even the Waymo dataset team [21], who made great efforts to overcome the above engineering difficulties, still suffered from several insuperable factors that affect the projection accuracy. For instance, the “rolling-shutter” effects due to high relative speed will cause significant deviation (fig. 2.a, fig. 2.b,), especially for side view cameras. Even trivial annotation inaccuracy on the 3D Lidar space leads to non-trivial projection misalignment (we highlight the gap by green in fig. 2.c for better illustration). Most importantly and most commonly, the vehicle is actually not a perfect cuboid shape (marked as green triangular corner for the left tail-lamp area in fig. 2.d). That is why most of the 3D box projections looks enlarged comparing to the actual image area even using the perfect 3D bounding box annotation. All above reasons jointly conclude that directly projecting the 3D bounding box are not enough for precise image-based learning tasks. As a result, the Waymo 2D [21] and NuImage [3] employ additional annotators to label image 2D bounding box for complementary. This “redundant” annotation efforts on both 3D and 2D space motivates this research. We argue that a properly trained neural network is capable of refining the projection misalignment caused by various reasons with very few 2D bounding box labels as guidance. That is, you only label once on the 3D Lidar point cloud, while image cuboids and 2D bounding boxes annotations are obtained automatically.

Our proposed network optimizes minimum parameters in 3D box based on Lidar annotation and aligns it with 2D images in an end-to-end way, where only the parameters that do not affect the potential collision relations between the target vehicle and the ego vehicle are refined. Specifically, the position of nearest vertex of the target 3D box is kept unchanged and only the peripheral vertexes are slightly refined by optimizing the corresponding dimension as fig. 4 illustrated, which are already enough to obtain an accurate image projection. Our method does not require the cuboid annotation for training but only uses 2d boxes as the guidance signal to ensure that our refined cuboids perfectly fit the actual 2D regions. In addition, we jointly train part of

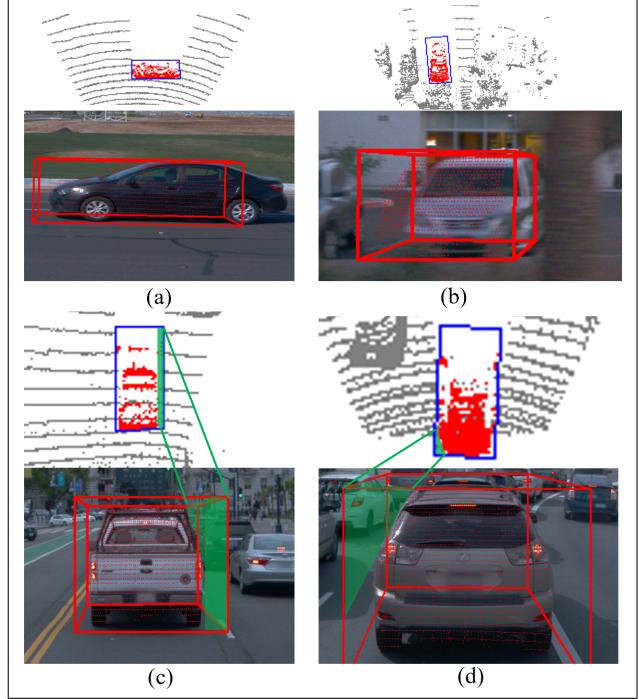


Figure 2. Examples where Lidar boxes cannot be used directly as cuboids. (a),(b): Significant deviation of rear-view images. (c): Misalignment brought by annotation inaccuracy. (d): Gaps because of vehicle shapes. We project the [Lidar points](#) to 2D images to show the position of Lidar objects, and use [green](#) to show the corresponding margins in 2D and 3D.

2D labeled images and a large amount of 2D unlabeled images in a semi-supervised manner. We test our approach on the Waymo [21] and NuScenes [3] and compare our method with traditional geometric solvers. The experiments prove that our method applies to various camera settings, such as front view, side view, and rear view, and is helpful to the training and application of subsequent perceptual tasks. To conclude, our contributions are as follows,

1. Introduce a collision relationship to solve the 3D-2D alignment problem based on Lidar bounding boxes, and enable the cuboid refinement process to operate in an end-to-end way.
2. Propose a semi-supervised method to train the refinement network to reduce requirements for ground-truth annotation during training.
3. Our method is the first to focus on image-level cuboid adaptation. The refinement result can work as the ground-truth value of perception tasks such as monocular 3D detection based on 2D images.

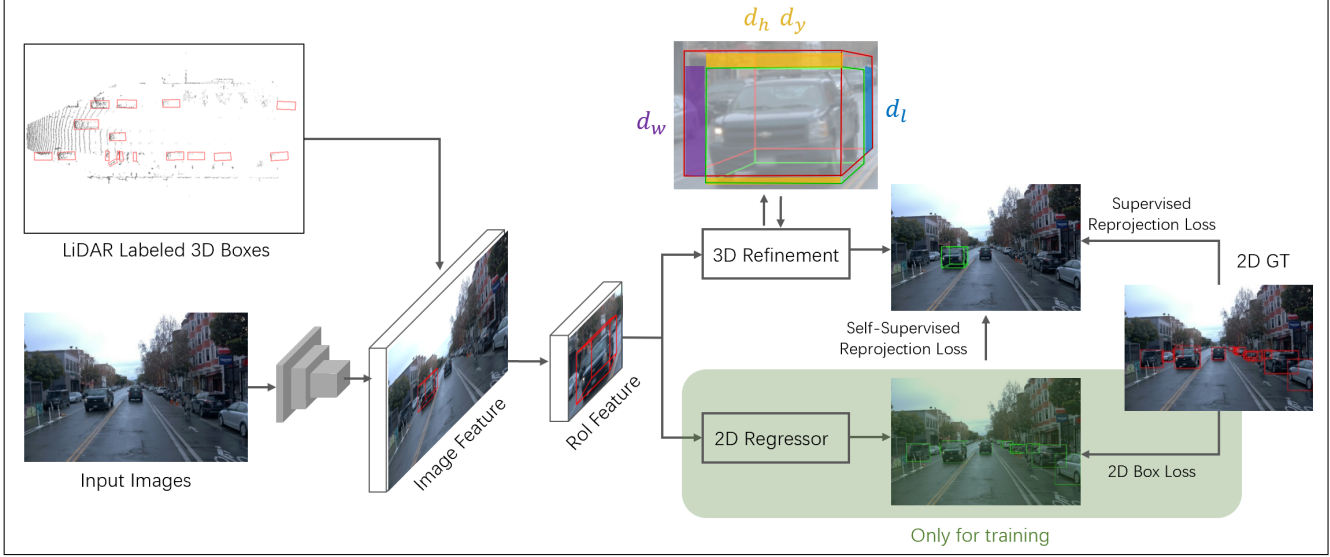


Figure 3. The framework of our network. We use a Faster-RCNN backbone(ResNet50) to extract pyramid feature maps from input 2D images, and use 3D Lidar annotations as proposals to crop out corresponding features. The features are then fed to two separate branches for refined 2D boxes and refined 3D cuboids. The 2D branch is only used to assist training and will not participate in the final inference.

2. Related Work

The auxiliary annotation system is an essential part of the closed loop for data processing in autonomous driving. This section briefly introduces the standard automated and semi-automated annotation methods based on Lidar and images.

2.1. Lidar-Centered Labeling Methods

Lidar-Centered labeling methods can further be divided into two kinds. The first is the reconstruction-based method targeting large statistic scenes, which is usually closely combined with establishing high-precision maps. Early researchers build a complete map of the large scene using the SLAM technology, filter out moving obstacles, and split the whole scenery into small segments for further semantic segmentation and annotation [2]. Recently, powered by the BEV-based fusion networks, researchers fuse Lidar point clouds with surrounding images in bird-eye view and integrate semantic segmentation, direction estimation, and some other tasks in a single network to produce a vectorized map [10, 12, 25]. By training a unified model suitable for multiple functions on small data sets with precise annotation, researchers can use a single model to label large amounts of data. However, the high requirements for training data and the generalization capability of multi-task models limit the usage of such annotation methods. This inspired some researchers to try simplifying high-precision maps by selecting different kinds objects as landmarks and creating semantic maps containing only specific semantic objects [11, 19]. Such semantic maps significantly reduce the previous training work, but lead to more limitations in accuracy and application scenarios.

The other kind of Lidar-based labeling focuses more on moving vehicles. Pioneers use human assistance to confirm the approximate anchor of objects and employ the pre-trained detection and segmentation network to label the objects [7]. Recently, researchers have tried to minimize the annotators' operation and select a coarse-to-fine method based on SOTA detection and tracking methods to label objects automatically. [18] first leverages a 3D detector to give out the object poses through the whole dataset and then associate objects across different frames using multi-object trackers. With the associated proposals, researchers can crop out the entire tracklets of each object and accumulate the point clouds for a refined 3D box. Similarly, [23] generates the initial trajectory of all objects and regresses the unchanged size and changing poses in different branches. Such labeling methods carries out further optimization to improve the accuracy of 3D boxes based on detection networks. Obviously, though succeeding in improving the labeling accuracy, they still rely on the pre-training on well-labeled datasets. [14] goes a step further, estimating a 3D scene flow of a sequence of Lidar frames and then accumulating the point clouds belonging to the same object. The researchers further perform shape registration to form 3D amodal bounding boxes as the ground-truth annotations. This method finally eliminates manual annotation, but it cannot deal with the vacancy and deformation caused by occlusion, rolling shutter and accumulation error of the optical flow. In addition, because this kind of labeling method focus more on Lidar box accuracy, it completely discards 2D information, and still cannot solve the problems of 3D-2D deviation in cuboid alignment tasks.

2.2. Image-Centered Labeling Methods

Considering the deviation of Lidar boxes in the image domain, some researchers have tried directly labeling without Lidar point clouds' assistance.

Image-based labeling methods, lacking the spatial information, usually rely on the network to predict the depth map or SDF information and then do the scene-level reconstruction or object-level annotation based on the predicted depth. One typical method is to predict object models using 2D images and supervise the reconstruction result with differentiable shape renderers [2, 4]. [2] pre-trains a 2D detection network on real data and a shape generation network on CAD datasets, and crops out the candidate objects, predicts the SDF of objects, and supervises the whole network using 2D rendering loss. This method avoids complex image depth and shape annotation for real-world data, but relies heavily on the CAD dataset used for pre-training. Following Tesla, researchers further try to create ground-truth annotation using Nerf [13] or improved implicit methods [26, 27] to avoid such pre-training procedures. However, both the shape generation network and the Nerf-based rendering network focus more on pixel-level recovering, and are too complex and resource-consuming for the perception task.

3. Problem Definition

Given the 3D Lidar annotation $B_{lidar} = \{x, y, z, h, w, l, ry\}$, we hope to extract a 3D cuboid B_{cuboid} that can align tightly with 2D objects with only 2D supervision signals $L_{2D} = \{x_{min}, y_{min}, x_{max}, y_{max}\}$. Such a problem, to optimize a 7-D feature with a 4-D loss, is ill-posed and can not be formulated well in theory. Therefore, our first task is to find more constraints or to keep some variables frozen during the refinement.

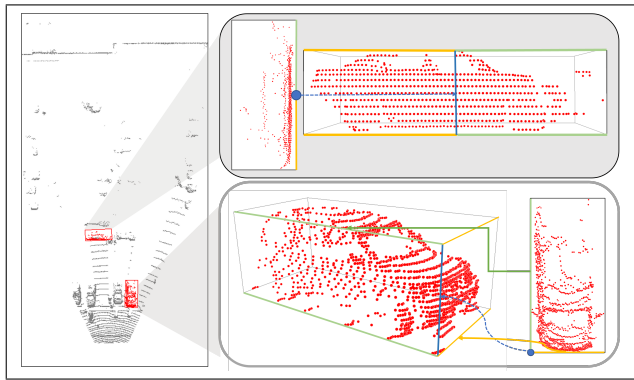


Figure 4. The \mathcal{L} -shape correspondence between Bev boxes and 3D boxes of Lidar point clouds. Lower: Cases with explicit \mathcal{L} -corners on 3D Boxes. Upper: Cases without \mathcal{L} -corners. We use blue to denote \mathcal{L} -corners, and use yellow and green to mark \mathcal{L} -edges.

To determine the frozen variables, we introduce the concept of *collision relationships*. The ultimate purpose of 3D

detection is to prevent collision between the sensor and objects, and such collision relationships are defined by the side of objects facing the sensor and the nearest point of the object from the sensor. The points closest to the sensor must be marked accurately in the 3D annotations, and slightly changing the locations of the peripheral points will not influence the downstream module to plan a collision-free trajectory. Therefore, to label an accurate B_{cuboid} while still keep the original *collision relationships*, we should first try to find the nearest point of the object, then expand the dimensions for each axis until the whole cuboid align with the expected contour.

As is shown in fig.4(lower), the contour of the point clouds forms a \mathcal{L} -shape, and the nearest point must be the corner of the \mathcal{L} . We define such corners as \mathcal{L} -corners and edges connected to the corners as \mathcal{L} -edges. The annotators first locate the \mathcal{L} -corner from the bird-eye-view and then draw three \mathcal{L} -edges starting from the point to form the height, width, and length of the 3D box in 3D view. On the premise of maintaining the same *collision relationship*, the horizontal position of this \mathcal{L} -corner should be accurate, reliable, and unchangeable in the adaptation process, and the \mathcal{L} -edges, which also affect the position and sizes of the objects, can be optimized to fit the 2D annotations. Thus, we fix the \mathcal{L} -corner, which corresponds to the horizontal coordinates of the vertical \mathcal{L} -edge, and change the length of three \mathcal{L} -edges during the refinement. Where the camera captures the vehicle from the front and the Lidar annotation has no \mathcal{L} -shapes, the *collision relationship* is determined by the horizontal position of the side of the object that faces the camera. Under such circumstances, the center of the nearest side is defined as the \mathcal{L} -corner, and the three edges connected to this point are the \mathcal{L} -edges to be optimized(fig. 4, upper). In conclusion, the final refinement target of our method is $D_{Lidar} = \{d_l, d_w, d_h, d_y\}$, where d_h and d_y together define the length of the vertical \mathcal{L} -edge.

It should be pointed out that the selection of \mathcal{L} -corner is only related to the original viewpoint between the target vehicle and the ego vehicle, and can be pre-calculated using 2D-3D correspondences. Following [8, 9], we calculate the projected 2D box and mark the left-down corner $l_d = \{x_d, y_d\}$ and the right-up corner $r_u = \{x_u, y_u\}$. We then tag the 3D corners of B_{lidar} and find the correspondence between the corners and the projected 2D boxes. In the example at fig 5, the x-coordinate x_d of left-down corner l_d corresponds with 3D corners 3 and 7, and the x-coordinate x_u of the right-up corner r_u corresponds with 3D corner 1 and 5. This id-correspondence means that our camera is located at the front-right side of the car(view 3).

Thus, our method can be formulated as

$$D_{Lidar} = F(\text{view}, \pi(B_{lidar}), I_{RGB}) \quad (1)$$

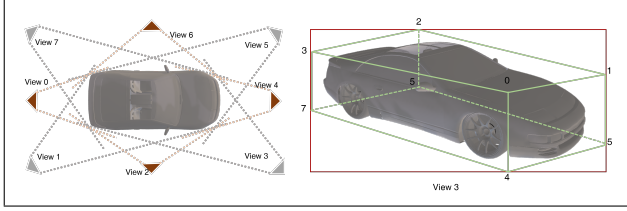


Figure 5. Left: We divide the camera-object relationship into eight different views and calculate the view through the projected 2D boxes. Right: The correspondence between the projected 2D box and 3D view 3. The x-coordinate of the 2D box is divided by 3D corners 3, 7 and corners 1, 5.

4. Method

4.1. Semi-Supervised Refinement Network

The cuboid refinement task is completed using a two-stage 2D detection network similar to faster-RCNN [20]. For a set of input data (B_{lidar}, I_{RGB}) , we first extract the 2D image feature f_{RGB} through a simple backbone network(ResNet50 in our experiments) and then project B_{lidar} to f_{RGB} to obtain the corresponding f_{Lidar} for 3D boxes. The projected 2D boxes are regarded as the proposals and, together with the f_{Lidar} , fed to a 2D RCNN network for refinement. As mentioned earlier, our network outputs four variables, namely $D_{Lidar} = \{d_l, d_w, d_h, d_y\}$. We use the sigmoid layer to ensure the output D_{Lidar} within the range of 0-2 to avoid excessive geometric deviation. The original 3D boxes are then refined by D_{Lidar} and projected to 2D again to B_{proj} for loss calculation.

Since our ultimate goal is to design a helpful labeling tool, the network should be able to conduct self-supervised refinement or semi-supervised refinement with as few 2D annotations as possible. Thus, we add an auxiliary 2D branch to the network to reduce or replace the demand for ground-truth data.

The simplest auxiliary method is to pre-train a separate 2D detection network and generate a 2D pseudo annotations as training signals. However, such training strategies causes a variety of waste. Since our 3D branches are also trained based on 2D images, the two networks can share the backbone, thus reducing the requirement for calculation. Meanwhile, different from traditional 2D detection tasks, the input 3D Lidar boxes are the only candidates to be refined, and the RPN stage of popular 2D networks is redundant. Under such consideration, we create an auxiliary branch that shares the same backbone with the 3D network, and takes the two-dimensional projection of the 3D box as proposals to extract 2D features. An RCNN network follows to refine the proposals for the optimized 2D box B_{gen} . This design allows us to train the entire network simultaneously when the ground-truth value exists and use the 2D branch

to train the 3D results when the 2D ground-truth value is missing. The efficiency of such a semi-supervision strategy is evaluated in Sec. 6.

4.2. Loss Function

During training, our network gives out the 2D predicted annotation B_{gen} and the 3D refinement parameter D_{Lidar} simultaneously. The 2D branch is trained following popular 2D detection networks as [20], and the 2D loss is

$$E_{2D} = \frac{1}{N_{box}} H(B_{gen} - L_{2D}) \quad (2)$$

, where H denotes the robust Huber loss.

The 3D projection loss is much more complicated than 2D. When an object is too close to the camera, usually the camera can only capture half of the object, while the other half is in the blind zones. In such a situation, the depth of the object in the camera coordinate system will undergo a negative-to-positive mutation, and the projection result may have an infinite value in the outermost edge, leading to a NaN in the training loss. Therefore, we calculate each edge of the projected box separately and supervise different edges in different situations. This also deals with 2D occlusion, where half of the object is occluded and the size can not be determined using 2D boxes. The 3D projection loss is formulated as

$$E_{3D} = \frac{1}{N_{box}} \sum_{i=0}^3 1_{e^i} H(1_{gt}(B_{proj}^i - L_{2D}^i) + 1_{!gt}(B_{proj}^i - B_{gen}^i)) \quad (3)$$

1_{e^i} is a 0-1 function indicating whether the i -the edge of the projected 2D box is legal. Similarly, 1_{gt} and $1_{!gt}$ show whether there is a ground-truth 2D box for training.

In addition, we set a consistency loss to ensure the consistency of the 3D network and prevent instability during training. For each input box B_{lidar} , a random set of variables $D_{aug} = \{d_l, d_w, d_u, d_d\}$ is generated to augment the input information to B'_{lidar} , and to give out the corresponding output D'_{Lidar} . If the refinement process of the network is robust enough, we can get $D_{Lidar} = D'_{Lidar} * D'_{aug}$. So during the training, there is

$$E_{con} = \frac{1}{N_{box}} H(D_{Lidar} - D'_{Lidar} * D_{aug}) \quad (4)$$

Therefore, the total loss tends to be

$$E_{total} = \lambda_1 1_{gt} E_{2D} + \lambda_2 E_{3D} + \lambda_3 E_{con} \quad (5)$$

5. Experiment

5.1. Experiment Setup

We use two public data sets, **Waymo** [21] and **NuScenes** [3], to test our cuboid annotation pipeline.

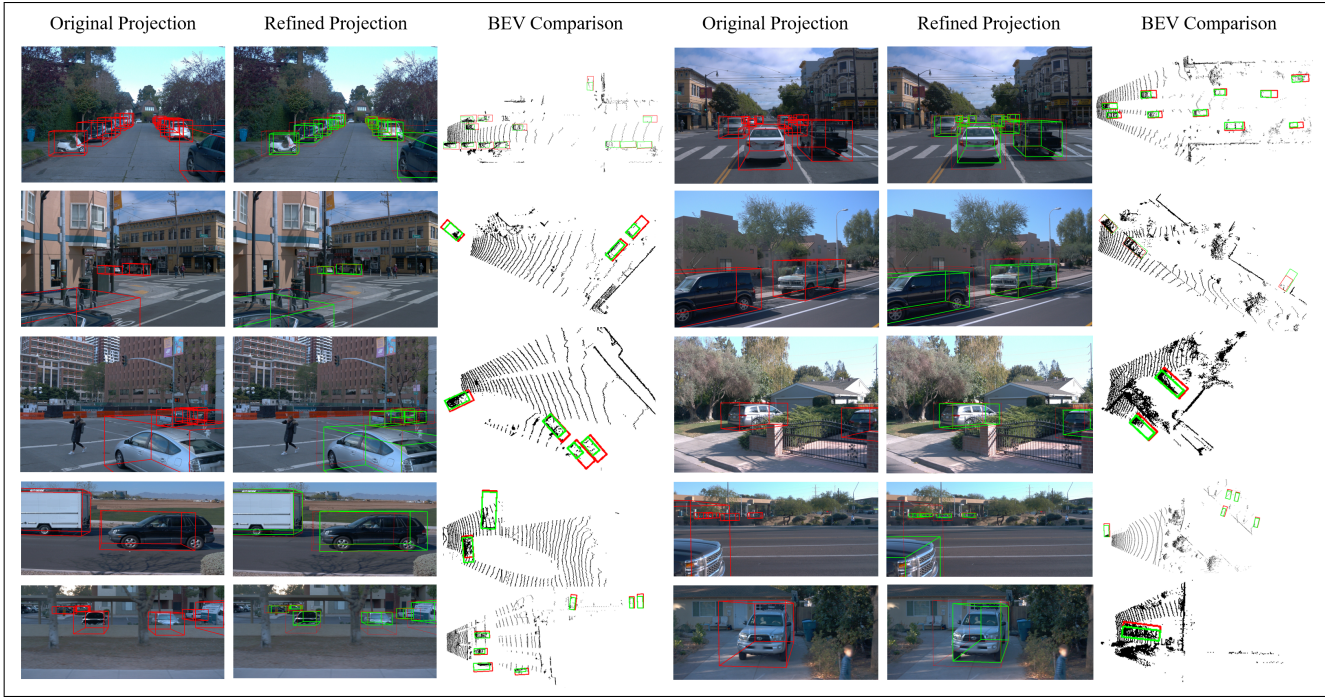


Figure 6. Refinement results on Waymo dataset. We use **red** to mark the 3D bounding boxes before refinement and **green** to show our optimized results. In order to better show the comparison before and after refinement, we additionally draw the original 3D projection upon our optimized 3D cuboids. We also draw the results in Bev view to show that our refined boxes are still reasonable in geometry. From up to down, we show the results from the front, left, right, rear-left, and rear-right cameras.

Waymo is an open automatic driving dataset containing more than 1,000 video sequences describing different driving scenes. Since there is no public benchmark for our 3D cuboid refinement task on the official test set, we use 798 official training sequences as our training set and 202 official validation sequences as our test set. Only the data corresponding to the VEHICLE tag is used in our experiments.

NuScenes is also a large-scale autonomous driving dataset with 3D object annotations. However, NuScenes does not provide dedicated 2D annotations but uses a separate 2D dataset, NuImages, as a complement. We take the Mask-RCNN [6] model provided by MMDetection [5] and trained in NuImages as an “annotator” to label 2D bounding boxes on NuScenes 3D dataset as ground truth for both training and testing phases.

Table 1. Difference between Waymo and NuScenes

Name	2D GT	3D GT	Uniform Size	Cam. Num.
Waymo	✓	✓	✗	5
NuScenes	✗	✓	✓	6

Metric. Considering there is no ground-truth cuboid annotation on both **Waymo** [21] and **NuScenes** [3], and our refinement does not change the key 3D properties of the labeled 3D bounding boxes as Sect. 3 described, we mainly

evaluate the refinement accuracy by the 2D IoU between the cuboid projection and the ground truth 2D boxes, and also the corresponding 2D recall.

During data preparation, we project the 3D boxes onto the 2D image and calculate the IOU between the projection and the 2D ground-truth(GT) annotation. After that, we use the Hungarian algorithm to match the two groups of boxes and remove the matching with IOU less than 0.3. Such matches are used as GT correspondences during training and testing. Unless otherwise specified, only one-third of training data is with 2D GT boxes as supervision and the rest are all self-supervised. We train our network for ten epochs from scratch with batch size 16. All the experiments are conducted on single GTX 1080 Ti GPU.

5.2. Refinement Accuracy

5.2.1 Results on the Waymo Val set

To cooperator with five cameras in the Waymo dataset, we pad all images into the same size for jointly training and testing. The average IOU and the recall with different thresholds are listed in Table 2. For each entry, we report the experiment results before and after the refinement together with the corresponding improvements. Considering that the refinement difficulty of five cameras varies a lot due to different relative motion, we present the evaluation results of

Table 2. IOU Precision For 2D Boxes Before and After Refinement($\frac{1}{3}$ 2D Annotations during training) on Waymo Val Set.

Orig/Refined	Front View	Left Side	Right Side	Left Back	Right Back	Average
Avg. IOU	0.665	0.630	0.625	0.619	0.590	0.639
	0.835	0.815	0.805	0.776	0.762	0.811
	+0.170	+0.185	+0.180	+0.157	+0.172	+0.172
Recall($\text{IOU} \geq 0.5$)	82.8%	76.5%	75.3%	73.3%	69.3%	78.0%
	96.3%	94.3%	94.0%	92.1%	91.1%	94.3%
	+13.5%	+17.8%	+18.7%	+18.8%	+21.8%	+16.3%
Recall($\text{IOU} \geq 0.7$)	48.8%	40.6%	39.8%	37.1%	29.6%	42.6%
	85.6%	80.6%	79.1%	73.3%	71.7%	80.4%
	+36.8%	+40.0%	+39.3%	+36.2%	+42.1%	+37.8%
Recall($\text{IOU} \geq 0.9$)	1.9%	0.9%	0.6%	1.4%	0.4%	1.3%
	41.8%	39.3%	35.1%	26.6%	20.9%	36.1%
	+39.9%	+38.4%	+34.5%	+25.2%	+20.5%	+34.8%

the front-view, side-view and rear-view cameras separately. It can be seen that we achieve an IOU improvement by 0.17 on average and ensure that over 70% of the rear-view boxes maintain a 70% overlap with 2D annotations, which significantly outperform the direct projection counterpart.

To compare the effectiveness of our refinement more qualitatively, we visualize the projection of the 3D boxes before and after refinement on both 2D images and BEV maps in figure 6. Obviously, our refinement algorithm can align 3D information with 2D images to provide a tight 3D cuboid while maintaining 3D rationality and collision relationships. In the most complex rear-view camera scenes, our method can still handle the significant deviation caused by high relative speed, and provides reasonable 3D cuboids.

5.2.2 Results on the NuScenes Val set

We repeat the experiment on NuScenes dataset using the same network structure and training parameters. After our refinement, the overlap ratio between 3D projection and 2D detection improves a lot. We believe that this can reflect the robustness of our network. Without changing the network structure, we can refine and re-label 3D datasets with different 2D-3D deviations and precision.

Table 3. IOU Precision For 2D Boxes Before and After Refinement($\frac{1}{3}$ 2D Annotations) on NuScenes Val Set.

Recall(IOU)	0.5	0.7	0.9	Avg.
Orig	90.1%	58.4%	3.4%	0.703
Refined	94.6%	80.9%	42.0 %	0.821
Diff.	+4.5%	+22.5%	+38.6%	+0.119

6. Ablation Study

6.1. Comparison with Traditional Solvers

Intuitively, our learned box refinement can be replaced by traditional methods. With manually labeled 2D boxes,

we can use traditional optimization solvers, such as the Nelder-Mead method [15] or the Constrained Optimization BY Linear Approximation(COBYLA) method [16, 17], to calculate the length, width, height, corner and other variables of the 3D box, and make the projection align well with 2D. We follow the same *collision relationship* in Sect. 3 to reduce the free variables to four, and then eliminate 3D branches to train our 2D branch network independently. This is equivalent to using a classic Faster-RCNN network and replacing its RPN module with projection of 3D lidar labels as the proposals. The traditional solvers employed to optimize 3D boxes from 2D detections are implemented by the SciPy [22] library. Similar to our learning-based method, the refinement variables are still $\{dl, dw, dh, dy\}$, and we set the upper and lower bound of the optimization algorithms to 2 and 0. However, we found that manually tuning the optimization strategy hardly balance best image-level alignment accuracy and minimum changes of the 3D variables. Our network based approach can properly handle different cameras and different viewpoints by learning a good semantic prior from image appearance.

To fully compare the difference between our method and the traditional solvers, we first conduct the standard experiments with $\frac{1}{3}$ 2D annotations on the whole Waymo dataset, and illustrate in figure. 7.a that our method achieves overall best performance in both 2D alignment accuracy and 3D IOU retaining. Since the full dataset is too large, we additionally use the front-view images for ablation experiments and show that our method can present more and more advantages than the optimization-based methods when the ground truth gradually reduces.

Besides the 2D overlap between cuboid projections and the 2D annotations (2D IOU and 2D Recall ($\text{IOU} \geq 0.5$)), we add the overlap between the cuboid and the input 3D Lidar boxes on 3D and BEV to show the changes between cuboids and the original input boxes. With the decrease of 2D annotations during training, the network tends to re-

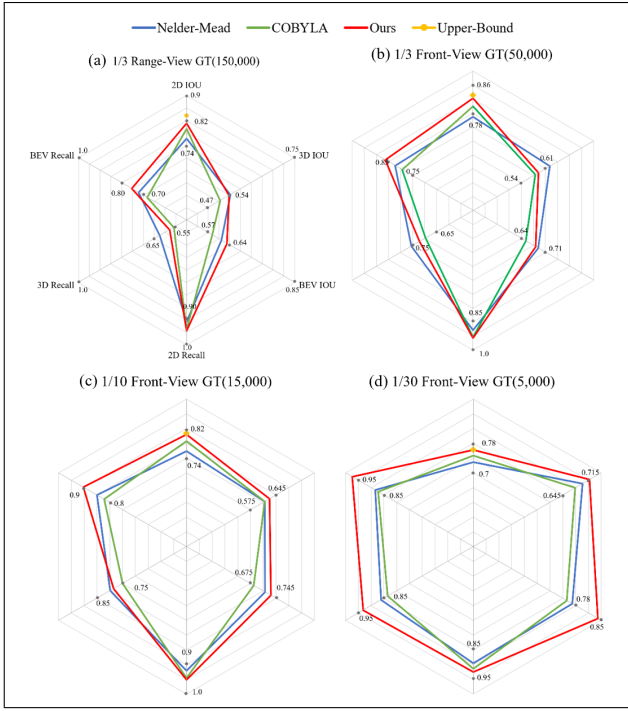


Figure 7. Radar maps showing the difference between our method and optimization solvers. (a): Model trained on the whole Waymo dataset with $\frac{1}{3}$ 2D GT annotations. (b),(c),(d): Model trained on the front-view camera with different numbers of 2D GT.

duce the modification of the input 2D projection(proposals). Therefore, the 3D and BEV indicators increase. In addition to this trend brought about by the 2D model, we can see two noticeable differences. First, our method always keeps much higher precision in 2D overlap and leads in BEV overlap, ensuring the best accuracy and avoiding the local minimum as optimization-based methods. Secondly, when the 2D GT data decreases, the 2D gap between the three methods narrows, and our method gradually gains advantages in the 3D overlap. This trend shows that when guidance information is insufficient, our method can obtain the maximum 2D accuracy through the minimum modification of the input box. It also reflects that our method requires less 2D annotations than traditional methods.

6.2. Semi-Supervision Still Works

As is mentioned in Sect. 4, we design a 2D branch and use 2D predictions as the supervision signal when lacking 2D annotations. To test the accuracy of such a semi-supervision strategy, we use the front-view data to do comparative experiments on the Waymo dataset. We randomly select $\frac{1}{3}$, $\frac{1}{5}$, $\frac{1}{10}$, $\frac{1}{30}$ 2D annotations for training respectively.

From Table 4, our auxiliary supervision method can obtain almost equivalent accuracy using 20% 2D annotations and can still stably optimize the 3D boxes when only 5000 2D annotations(1/30) are used. This proves the accuracy of

Table 4. IOU Precision For Cuboid Projections with Different Amount of 2D GT Annotations

2D GT	100%	33.33%	20%	10%	3.33%
Avg. IOU	0.825	0.822	0.815	0.803	0.763
Recall(0.5)	95.9%	95.7%	95.9%	95.3%	93.2%
Recall(0.7)	83.9%	83.5%	82.3%	80.1%	73.0%
Recall(0.9)	37.9%	36.0%	32.5%	27.9%	13.1%

our semi-supervision strategy in the absence of 2D annotations. It also shows that our network can reduce the demand for labeled data as much as possible.

6.3. Consistency Loss for Training

Our consistency loss hopes to ensure that different 3D boxes corresponding to the same 2D object are regressed to the same output. To test the efficiency of this loss function, we use the 2D IOU to evaluate the training results based on small amounts of 2D annotations.

Table 5. IOU Difference For Cuboid Projections with and without Consistency Loss

GT Num.	Avg. IOU	Recall(0.5)	Recall(0.9)
33.33%	+0.02	+0.0%	+1.3%
10%	+0.14	+0.2%	+2.4%
3.33%	+0.07	+0.7%	+3.1%

Our consistency loss further boosts the performance of the network with fewer 2D annotations. This is in line with the original intention of our loss design, that is, to ensure the robustness of the network training process and the consistency of the output results, and to assist the network to converge when 2D annotations are insufficient.

7. Conclusions and Discussions

We propose a semi-supervised label refinement method, which can replace the manual adjustment process and convert a 3D box based on Lidar into a 3D cuboid based on the camera. Our method takes *collision relationships* as the starting point and uses the \mathcal{L} -corners of objects to reduce free variables. With a light-weight 2D auxiliary branch and a simple consistency loss, we manage to conduct semi-supervised training with a small number of 2D GT annotations. Experiments show that our method can produce human-level annotations and deal with various 2D-3D deviation errors efficiently and accurately.

Limitations. Our method still requires a robust 3D box as input to reduce free variables by using accurate \mathcal{L} -shape information. When there are severe calibration errors, and there is no overlap between 3D projections and 2D boxes, we cannot hold the geometric assumption of collision points.

References

[1] Adel Ahmadyan, Liangkai Zhang, Artsiom Ablavatski, Jianing Wei, and Matthias Grundmann. Objectron: A large scale dataset of object-centric videos in the wild with pose annotations. In *Proceedings of the IEEE/CVF conference on computer vision and pattern recognition*, pages 7822–7831, 2021. 1

[2] Daan Bloembergen and Chris Eijgenstein. Automatic labelling of urban point clouds using data fusion. *ArXiv*, abs/2108.13757, 2021. 3, 4

[3] Holger Caesar, Varun Bankiti, Alex H. Lang, Sourabh Vora, Venice Erin Liou, Qiang Xu, Anush Krishnan, Yu Pan, Giancarlo Baldan, and Oscar Beijbom. nuscenes: A multimodal dataset for autonomous driving. *2020 IEEE/CVF Conference on Computer Vision and Pattern Recognition (CVPR)*, pages 11618–11628, 2020. 1, 2, 5, 6

[4] Wenzheng Chen, Jun Gao, Huan Ling, Edward Smith, Jaakko Lehtinen, Alec Jacobson, and Sanja Fidler. Learning to predict 3d objects with an interpolation-based differentiable renderer. *ArXiv*, abs/1908.01210, 2019. 4

[5] MMDetection3D Contributors. MMDetection3D: Open-MMLab next-generation platform for general 3D object detection. <https://github.com/open-mmlab/mmdetection3d>, 2020. 6

[6] Kaiming He, Georgia Gkioxari, Piotr Dollár, and Ross B. Girshick. Mask r-cnn. *IEEE Transactions on Pattern Analysis and Machine Intelligence*, 42:386–397, 2020. 6

[7] Jungwook Lee, Sean Walsh, Ali Harakeh, and Steven L. Waslander. Leveraging pre-trained 3d object detection models for fast ground truth generation. *2018 21st International Conference on Intelligent Transportation Systems (ITSC)*, pages 2504–2510, 2018. 3

[8] Peiliang Li, Xiaozhi Chen, and Shaojie Shen. Stereo r-cnn based 3d object detection for autonomous driving. *2019 IEEE/CVF Conference on Computer Vision and Pattern Recognition (CVPR)*, pages 7636–7644, 2019. 4

[9] Peiliang Li, Tong Qin, and Shaojie Shen. Stereo vision-based semantic 3d object and ego-motion tracking for autonomous driving. In *ECCV*, 2018. 4

[10] Qi Li, Yue Wang, Yilun Wang, and Hang Zhao. Hdmapnet: An online hd map construction and evaluation framework. *2022 International Conference on Robotics and Automation (ICRA)*, pages 4628–4634, 2022. 3

[11] Ziwei Liao, Jieqi Shi, Xianyu Qi, Xiaoyu Zhang, Wei Wang, Yijia He, Ran Wei, and Xiao Liu. Coarse-to-fine visual localization using semantic compact map. *2020 3rd International Conference on Control and Robots (ICCR)*, pages 30–37, 2020. 3

[12] Yicheng Liu, Yue Wang, Yilun Wang, and Hang Zhao. Vectormapnet: End-to-end vectorized hd map learning. *ArXiv*, abs/2206.08920, 2022. 3

[13] Ben Mildenhall, Pratul P. Srinivasan, Matthew Tancik, Jonathan T. Barron, Ravi Ramamoorthi, and Ren Ng. Nerf: Representing scenes as neural radiance fields for view synthesis. In *ECCV*, 2020. 4

[14] Mahyar Najibi, Jingwei Ji, Yin Zhou, C. Qi, Xinchen Yan, Scott M. Ettinger, and Drago Anguelov. Motion inspired unsupervised perception and prediction in autonomous driving. *ArXiv*, abs/2210.08061, 2022. 3

[15] John A. Nelder and Roger Mead. A simplex method for function minimization. *Comput. J.*, 7:308–313, 1965. 7

[16] M. J. D. Powell. Direct search algorithms for optimization calculations. *Acta Numerica*, 7:287 – 336, 1998. 7

[17] M. J. D. Powell. A view of algorithms for optimization without derivatives 1. 2007. 7

[18] C. Qi, Yin Zhou, Mahyar Najibi, Pei Sun, Khoa T. Vo, Boyang Deng, and Dragomir Anguelov. Offboard 3d object detection from point cloud sequences. *2021 IEEE/CVF Conference on Computer Vision and Pattern Recognition (CVPR)*, pages 6130–6140, 2021. 1, 3

[19] Tong Qin, Yuxin Zheng, Tongqing Chen, Yilun Chen, and Qing Su. A light-weight semantic map for visual localization towards autonomous driving. *2021 IEEE International Conference on Robotics and Automation (ICRA)*, pages 11248–11254, 2021. 3

[20] Shaoqing Ren, Kaiming He, Ross B. Girshick, and Jian Sun. Faster r-cnn: Towards real-time object detection with region proposal networks. *IEEE Transactions on Pattern Analysis and Machine Intelligence*, 39:1137–1149, 2015. 5

[21] Pei Sun, Henrik Kretzschmar, Xerxes Dotiwalla, Aurelien Chouard, Vijaysai Patnaik, Paul Tsui, James Guo, Yin Zhou, Yuning Chai, Benjamin Caine, Vijay Vasudevan, Wei Han, Jiquan Ngiam, Hang Zhao, Aleksei Timofeev, Scott M. Ettinger, Maxim Krivokon, Amy Gao, Aditya Joshi, Yu Zhang, Jonathon Shlens, Zhifeng Chen, and Dragomir Anguelov. Scalability in perception for autonomous driving: Waymo open dataset. *2020 IEEE/CVF Conference on Computer Vision and Pattern Recognition (CVPR)*, pages 2443–2451, 2020. 1, 2, 5, 6

[22] Pauli Virtanen, Ralf Gommers, Travis E. Oliphant, Matt Haberland, Tyler Reddy, David Cournapeau, Evgeni Burovski, Pearu Peterson, Warren Weckesser, Jonathan Bright, Stéfan J. van der Walt, Matthew Brett, Joshua Wilson, K. Jarrod Millman, Nikolay Mayorov, Andrew R. J. Nelson, Eric Jones, Robert Kern, Eric Larson, C J Carey, Ilhan Polat, Yu Feng, Eric W. Moore, J. Vanderplas, Dennis Laxalde, Josef Perktold, Robert Cimrman, Ian Daniel Henriksen, E. A. Quintero, Charles R. Harris, Anne M. Archibald, Antônio H. Ribeiro, Fabian Pedregosa, Paul van Mulbregt, Aditya Alessandro Pietro Alex Andreas Andreas Anthony Ant Vijaykumar Bardelli Rothberg Hilboll Kloeckner Sco, Aditya Vijaykumar, Alessandro Pietro Bardelli, Alex Rothberg, Andreas Hilboll, Andre Kloeckner, Anthony M. Scopatz, Antony Lee, Ariel S. Rokem, C. Nathan Woods, Chad Fulton, Charles Masson, Christian Häggström, Clark Fitzgerald, David A. Nicholson, David R. Hagen, Dmitrii V. Pasechnik, Emanuele Olivetti, Eric Martin, Eric Wieser, Fabrice Silva, Felix Lenders, Florian Wilhelm, Gert Young, Gavin A. Price, Gert-Ludwig Ingold, Gregory E. Allen, Gregory R. Lee, Hervé Audren, Irvin Probst, Jorg P. Dietrich, Jacob Silterra, James T. Webber, Janko Slavić, Joel Nothman, Johannes Buchner, Johannes Kulick, Johannes L. Schönberger, José Vinícius de Miranda Cardoso, Joscha Reimer, Joseph E. Harrington, Juan Rodríguez, Juan

Nunez-Iglesias, Justin Kuczynski, Kevin Lee Tritz, Martin Dr Thoma, Matt Newville, Matthias Kümmerer, Maximilian Bolingbroke, Michael Tartre, Mikhail Pak, Nathaniel J. Smith, Nikolai Nowaczyk, Nikolay Shebanov, Oleksandr Pavlyk, Per Andreas Brodtkorb, Perry Lee, Robert T. McGibbon, Roman Feldbauer, Sam Lewis, Sam Tygier, Scott Sievert, Sebastiano Vigna, Stefan Peterson, Surhud More, Tadeusz Pudlik, Taku Oshima, Thomas J. Pingel, Thomas P. Robitaille, Thomas Spura, Thouis Raymond Jones, Tim Cera, Tim Leslie, Tiziano Zito, Tom Krauss, U. Upadhyay, Yaroslav O. Halchenko, and Y. Vázquez-Baeza. Scipy 1.0: fundamental algorithms for scientific computing in python. *Nature Methods*, 17:261 – 272, 2020. [7](#)

[23] Binh Yang, Min Bai, Ming Liang, Wenyuan Zeng, and Raquel Urtasun. Auto4d: Learning to label 4d objects from sequential point clouds. *ArXiv*, abs/2101.06586, 2021. [1](#), [3](#)

[24] Sergey Zakharov, Wadim Kehl, Arjun Bhargava, and Adrien Gaidon. Autolabeling 3d objects with differentiable rendering of sdf shape priors. *2020 IEEE/CVF Conference on Computer Vision and Pattern Recognition (CVPR)*, pages 12221–12230, 2020. [2](#)

[25] Yunpeng Zhang, Zheng Hua Zhu, Wenzhao Zheng, Junjie Huang, Guan Huang, Jie Zhou, and Jiwen Lu. Beverse: Unified perception and prediction in birds-eye-view for vision-centric autonomous driving. *ArXiv*, abs/2205.09743, 2022. [3](#)

[26] Shuaifeng Zhi, Tristan Laidlow, Stefan Leutenegger, and Andrew J. Davison. In-place scene labelling and understanding with implicit scene representation. *2021 IEEE/CVF International Conference on Computer Vision (ICCV)*, pages 15818–15827, 2021. [4](#)

[27] Shuaifeng Zhi, Edgar Sucar, André Mouton, I. Haughton, Tristan Laidlow, and Andrew J. Davison. Ilabel: Interactive neural scene labelling. 2021. [4](#)